In situ probing of magnetron sputtered Pt-Ni alloy fuel cell catalysts during accelerated durability test using EC-AFM

CrossMark

Ivan Khalakhan[a,*], Mykhailo Vorokhta[a], Peter Kúš[a], Milan Dopita[b], Michal Václavů[a], Roman Fiala[a], Nataliya Tsud[a], Tomáš Skála[a], Vladimír Matolín[a]

[a] Charles University, Faculty of Mathematics and Physics, Department of Surface and Plasma Science, V Holešovičkách 2, 18000, Prague 8, Czech Republic
[b] Charles University, Faculty of Mathematics and Physics, Department of Condensed Matter Physics, Ke Karlovu 5, 121 16, Prague 2, Czech Republic

A R T I C L E   I N F O

A B S T R A C T

As-deposited Pt-Ni and annealed Pt-Ni alloy catalyst films prepared by magnetron co-sputtering were investigated in order to quantify their ageing during accelerated durability test. The parameters of the durability test were chosen to simulate severe potential conditions that may occur at start-up/shut-down cycles of a fuel cell. Using *in situ* electrochemical atomic force microscopy complemented with *ex situ* energy dispersive X-ray spectroscopy, X-ray photoelectron spectroscopy, synchrotron radiation photoelectron spectroscopy and X-ray diffraction provided step-by-step correlation of chemical and morphology changes induced by catalyst's aging processes. We show that the as-deposited Pt-Ni films face severe chemical stability problem which leads to almost complete destruction of the alloy during the durability test. On the other hand Pt-Ni films annealed in vacuum are more resistive to morphological and chemical changes. It was confirmed that upon annealing due to redistribution of Pt and Ni atoms Pt-skin is formed on catalyst surface, which is responsible for a better stability during the aging test.

1. Introduction

Huge boost in global energy demand together with a strong dependence on fossil fuels lead to growing importance of development of alternative sources of clean energy. Among many candidates, proton exchange membrane fuel cells (PEMFCs) are one of the most promising due to high efficiency and low environmental pollution. They are expected to become a major power source for various applications [1]. To date, among other obstacles, such as fuel production and storage, the commercialization of such fuel cells is limited by slow kinetics of the oxygen reduction reaction (ORR), which occurs at cathode. Another barrier is high cost of platinum, which still remains the only ORR catalyst that meets catalysis/durability requirements. Extensive studies have been performed in order to overcome aforementioned limitations by searching for ORR catalyst that would be more active, less expensive and more stable than pure platinum. So far, one of the most promising strategies is alloying of platinum with relatively cheap transition metals. It has been reported that Pt alloyed with Ni, Co or Fe enhances the electrocatalytic activity

toward ORR [2–6], while at the same time it lowers catalyst cost due to reduction of the amount of used platinum. Activity improvement in such binary alloys has been explained through changes in oxygen binding energy, which is mainly caused by modification of the electronic structure of platinum [7,8]. Furthermore, the ability to tune atomic arrangement in alloys by producing so-called Pt-skin [8–10], Pt-skeleton [9,11] and core shells [12–14] even further improved the catalyst efficiency.

Despite these improvements in activity, binary-alloy catalysts were found to be unstable at fuel cell operation conditions. Transition metals tend to dissolve in the acidic fuel cell environment, leading to catalyst dealloying, followed by a significant reduction of its activity during operation. In fact, Dubau et al. performed series of tests over Pt_3Co catalysts, showing that during long-term operations of PEMFCs, severe degradation of cathode catalyst takes place [15,16] due to continuous Co dissolution. Furthermore, Pt-Ni, Pt-Fe and Pt-Co degradation was also investigated in numerous studies [17–22]. Despite intensive work, full knowledge about the time evolution of the structural and compositional changes in alloy catalyst during its degradation remains missing. This is mainly because majority of studies investigated catalysts only before and after reaction [17–19,23,24]. As a result, the knowledge about time-dependent evolution of catalysts during reaction is superficial. That is why operando

* Corresponding author.
E-mail address: khalakhan@gmail.com (I. Khalakhan).

techniques are becoming increasingly important to complement *ex situ* characterization methods [25]. Rising of modern techniques provides much better insight into the degradation mechanisms of cathode electrocatalysts, by measuring *in situ,* under conditions close to its real operation environment [20–22,26–29].

Potential that catalyst normally faces during steady-state fuel cell operation is around 1 V, however, higher potentials are unavoidable at, for example, startup/shutdown conditions [27,30]. While a majority of studies investigate the catalyst aging at conditions close to a standard fuel cell operation, it is of high importance to reveal catalyst behavior also under much harsher conditions. In our previous paper, we showed that Pt-Co catalyst faced severe degradation during electrochemical cycling to high potentials, which led to almost complete destruction of the alloy [27]. Herein, we investigate the behavior of as-deposited and vacuum annealed Pt-Ni bimetallic electrocatalysts, prepared by magnetron sputtering, during an accelerated durability test (ADT), which consists of 2000 repetitive potential sweeps from 0 to 1.3 V_{RHE}. By using the advanced EC-AFM technique, simultaneously utilizing cyclic voltammetry and AFM imaging at the electrode/ electrolyte interface, it is possible to monitor reactions on the surface of catalyst and track morphological changes at the same time. This enables correlation of structural changes with morphology changes, induced by catalysts aging processes. In combination with *ex situ* energy dispersive X-ray spectroscopy (EDX), X-ray diffraction (XRD) and synchrotron radiation photoelectron spectroscopy (SRPES) a comprehensive picture of the alloy behavior has been achieved.

2. Experimental

2.1. Samples preparation

Non-reactive magnetron sputtering was used to deposit Pt-Ni bimetallic catalyst and reference Pt films on freshly cleaved highly oriented pyrolytic graphite (HOPG, Bruker). HOPG was used as a substrate suitable for EC-AFM measurements due to its flat surface and high conductivity. It also mimics real carbon-based catalyst supports used in PEMFCs. The Pt-Ni catalyst was deposited by means of two magnetrons working simultaneously. For Ni sputtering we used a 2- inch diameter target installed on a TORUS UHV magnetron (Kurt J. Lesker) at a distance of 90 mm from the substrates. The radio-frequency power (13.56 MHz) applied to the Ni target was 25 W. For Pt sputtering we used the second home-

built DC magnetron at a distance of 200 mm from the substrate, tilted by 45° relative to the Ni target and the power applied was 20 W. Before starting the deposition the sputtering chamber was evacuated to 2×10^{-4} Pa. The sputtering was carried out in Ar atmosphere with total pressure of 4×10^{-1} Pa, giving a growth rate of Pt-Ni films of 3 nm min^{-1}. The total thickness of the films used in the present study was 10 nm. Annealing of Pt-Ni films was done in an ultra-high vacuum chamber (10^{-8} Pa) at 773 K for 10 min.

2.2. Ex situ samples characterization

Morphology of catalysts was examined by means of scanning electron microscopy (SEM), using MIRA 3 microscope (Tescan) at 30 keV electron beam energy. Chemical composition analysis was made using energy dispersive X-ray spectroscopy (EDX), X-ray photoelectron spectroscopy (XPS), and synchrotron radiation photoelectron spectroscopy (SRPES). EDX was carried out using Bruker XFlash detector mounted directly into SEM. XPS was performed in an ultrahigh vacuum (UHV) experimental chamber, operating at base pressures 10^{-8} Pa and equipped with SPECS Phoibos MCD 9 electron energy analyzer and a dual Mg/Al X-ray source. The high resolution SRPES was performed at the Materials Science Beamline at the Elettra synchrotron light source in Trieste, Italy. The beamline uses plane grating monochromator, providing the narrow band synchrotron light in the energy range of 21– 1000 eV.

X-ray diffraction (XRD) was used to obtain the detailed structural information about the investigated layers. XRD measurements were performed using Pananalytical MRD diffractometer equipped with parabolic multilayer mirror in the primary beam, and a long soller slit collimator (acceptance 0.27°), graphite monochromator and scintillation counter in the diffracted beam. The measurements were done in the parallel beam geometry (glancing angle X-ray diffraction geometry – GAXRD). In this geometry the penetration depth of X-ray does not significantly vary with the diffraction vector length, however, it strongly depends on the incidence angle of the primary beam. To be sure to get the maximum possible information from the investigated layer, the small constant incidence angle of the primary beam (γ = 1.5°) was used for measurements. All measurements were done using the CuKα radiation (λ = 0.15418 nm). The measured diffraction patterns were fitted using the whole powder pattern refinement method (Rietveld method). The measured XRD data revealed the phase composition and the lattice parameters of Pt-Ni phase. The
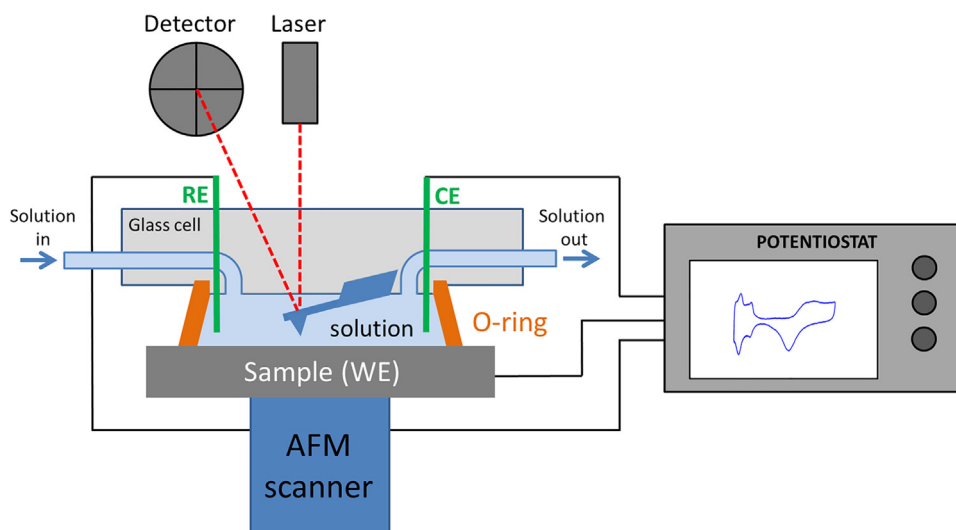

Fig. 1. Schematic illustration of a Bruker Multimode 8 EC-AFM.

MStruct software [31] was used for the fitting of the measured diffraction patterns.

2.3. In situ samples characterization

In situ electrochemical measurements were performed using a Bruker Multimode 8 EC-AFM. The sample was mounted on the AFM head, into a closed electrochemical liquid cell with approximately 50 μl of inner volume (see schematic illustration in Fig. 1). The liquid cell contained a three-electrode system, including the sample as a working electrode, high purity Pt wire (Safina, 99.99%) as a counter electrode and miniature leak-free Ag/AgCl (Innovative Instruments, Inc, 3.4 M KCl) as a reference electrode. For comparability with other results, we refer all measured potentials in this work to the reversible hydrogen electrode (RHE). The cell has a pipes attached to it through which the solution goes in and out. The electrochemical cell was filled with N_2-purged 0.1 M H_2SO_4 solution, prepared using deionized water (18.5 MΩ) and H_2SO_4 acid (Sigma Aldrich, 95%). Accelerated durability test was performed by 2000 repetitive potential sweeps between 0 V and 1.3 V versus RHE at a scan rate of 500 mV s^{-1} at room temperature. We did not include first cycle because it might be affected by the oxygenated adsorbates on the sample surface (samples were transferred from magnetron sputtering chamber to EC-AFM through air) and thus might be not reliable. The first cycle, thus, was considered as a cleaning procedure.

ScanAsyst AFM operation regime and Bruker ScanAsyst-Fluid+ probes were used for *in situ* recording of the sample morphology. After reaching a pre-determined number of electrochemical cycles, the cycling was temporarily stopped and AFM images were acquired in order to monitor surface morphology variations induced by the ADT.

3. Results and discussion

3.1. Characterization of as-deposited and annealed Pt-Ni catalyst films

SEM images of the Pt-Ni coated HOPG before and after annealing are presented in Fig. 2a and b, respectively. It can be seen that as-deposited Pt-Ni film is composed of small merely distinguishable grains. Upon annealing, the film tends to form a cracked structure. The bulk catalyst composition of $Pt_{0.53}Ni_{0.47}$ was calculated from EDX spectrum shown in Fig. S1.

SRPES Ni 2p and Pt 4f spectra of the as-deposited Pt-Ni sample and Pt-Ni after vacuum annealing are shown in Figs. 2c and d, respectively. By tuning the excitation energy of photons (E_p) the
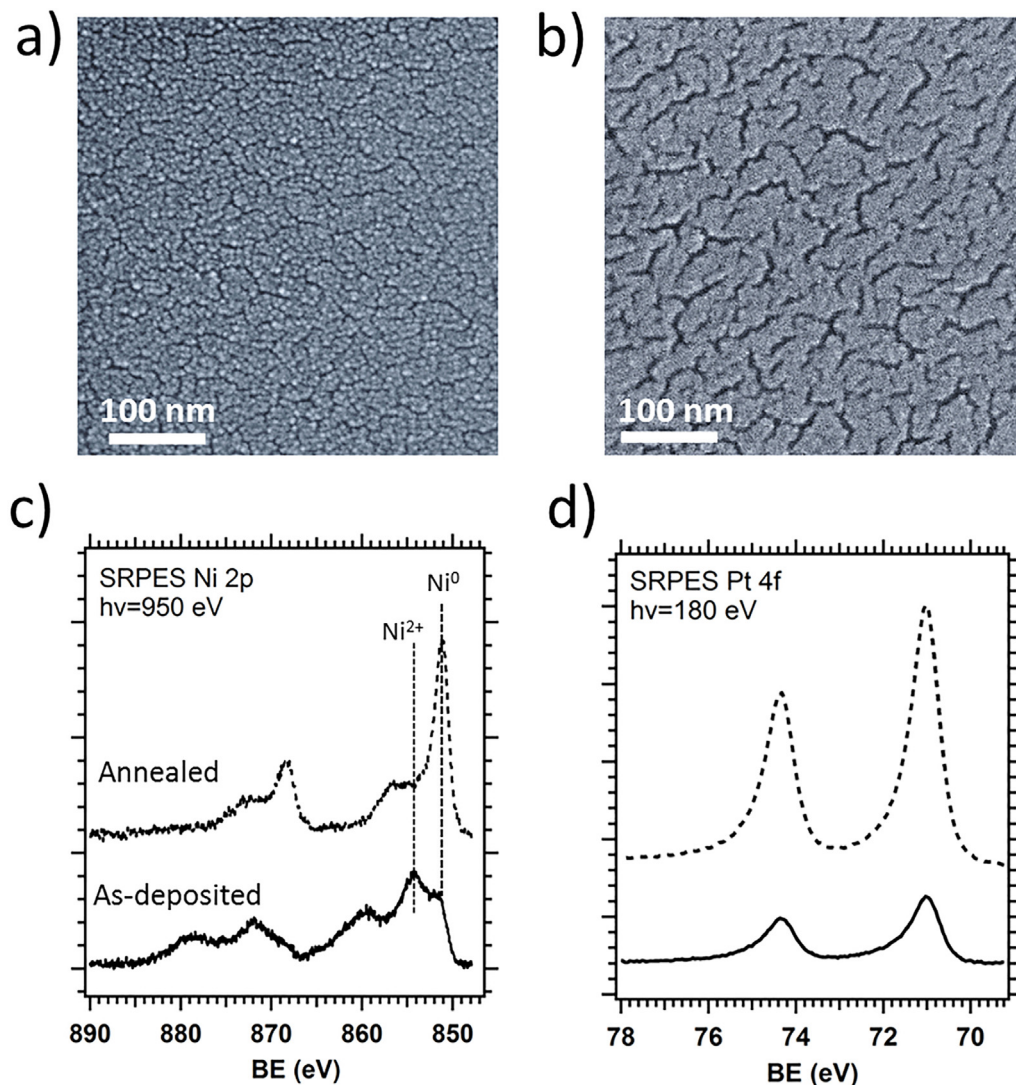
Fig. 2. SEM images of (a) as-deposited Pt-Ni film and (b) annealed Pt-Ni film; SRPES (c) Ni 2p and (d) Pt 4f spectra of as-deposited (solid line) and annealed (dashed line) Pt-Ni film.

kinetic energy of escaping photoelectrons can be set to a value ensuring the highest surface sensitivity to investigate any top-surface changes caused by annealing. The excitation energies for both Pt 4f and Ni 2p peaks were set to 180 eV and 950 eV respectively, ensuring the resulting kinetic energies of photoelectrons to be 100 eV. With that energy the surface probing depth is around 5–7 Å corresponding to about two top atomic layers.

Prior to annealing, the measured Ni 2p spectrum of as-prepared Pt-Ni catalyst (Fig. 2c bottom spectrum) is characteristic for partially oxidized Ni. It consists of three well defined characteristic doublets: predominant Ni^{2+} species at binding energy (BE) of about 854–872 eV, a satellite of Ni^{2+} at 859–879 eV and metallic component at 851-868.5 eV [32,33]. After precise fitting the satellite at about 857–877 eV of metallic Ni should be also seen, however, due to the low intensity it is lost among the signal from Ni^{2+}. Indeed, it is evident that amount of nickel oxides in the as-deposited Pt-Ni catalyst is substantially higher relative to Ni-metal content. This occurs because Ni must have been oxidized on the surface of the Pt-Ni catalyst by ambient atmosphere during transfer of the sample through air into the spectrometers for *ex situ* PES measurements. The presence of oxides was also proved in O 1s spectrum of the as-deposited sample (Fig. S2). After annealing in vacuum (Fig. 2c upper spectrum), the oxide peaks in the Ni 2p spectrum vanished and the metallic component became dominant. Moreover, no peak was detected in the O1s spectrum of the annealed Pt-Ni, shown in Fig. S2, evidencing complete disappearance of oxygen from the surface of annealed sample.

The Pt 4f spectra shown in Fig. 2d, for both as-deposited (bottom spectrum) and annealed (upper spectrum) samples consist of typical doublet at BE of 71-74.4 eV, corresponding to metallic platinum [33]. The only difference between the spectrum before and after the annealing is the intensity. After annealing Pt 4f peak increased substantially (by the factor of 3), while Ni 2p peak intensity remained about the same (Fig. 2c). Rise of Pt signal means that annealing led to the redistribution of the Pt and Ni on the surface of catalyst, i.e., Pt segregation on the surface and a formation of so-called Pt-skin over Pt-Ni alloy. Along with the increase of Pt signal a decrease of Ni 2p peak can be expected due to

Ni signal attenuation by the Pt-skin. However, as was shown above, the intensity of Ni 2p remained roughly the same before and after annealing. It could be explained by presence of nickel-bound oxygen atoms on the surface before annealing that attenuate the signal similarly to the Pt-skin after annealing.

The XRD technique was applied to get an information on the structure of crystalline phases present in the investigated layers. The parts of measured XRD patterns obtained for as-deposited and annealed Pt-Ni films are shown in Fig. S3. The XRD measurements confirmed, that the layers dominantly consist of one crystalline phase – face centered cubic (fcc) Pt-Ni (space group F m-3m). Additional, relatively sharp peaks visible in Fig. S3 originate from graphite, which is in form of randomly oriented grains, as a minor fraction, present in *00l* oriented HOPG substrate. The diffraction peaks of investigated Pt-Ni layers are shifted towards higher diffraction angles in comparison with the (111) Pt peak marked in Fig. S3. This corresponds to smaller lattice parameter of Pt-Ni layer compared to the one of pure Pt and indicates the alloy structure (Pt-Ni solid solution) of both as-deposited and annealed Pt-Ni films. According to Vegard's law, the lattice of a bimetallic alloy contracts with the increase of the element with smaller atomic radius. Since the radius of Ni is smaller than Pt, the increase of the Ni content results in decrease of the lattice parameter of Pt-Ni alloy. The shift of the (111) diffraction peak and consequently the shrinkage of the lattice parameter, originating from higher amount of Ni in Pt-Ni lattice is significantly more pronounced in the annealed sample [34]. The Pt-Ni catalyst elemental composition was estimated, using the Vegard's law, from lattice parameters, refined from measured XRD patterns. For annealed Pt-Ni the composition was calculated to be $Pt_{0.52}Ni_{0.48}$, which perfectly matches the composition measured by EDX, indicating a high degree of alloying. In turn, for as-deposited Pt-Ni sample the composition was estimated to be $Pt_{0.78}Ni_{0.22}$, which differs from the composition calculated using EDX. Most likely, the observed difference can be explained by the formation of amorphous Ni-oxide phase, which was measured on the as-deposited Pt-Ni sample by SRPES (Fig. 2c).
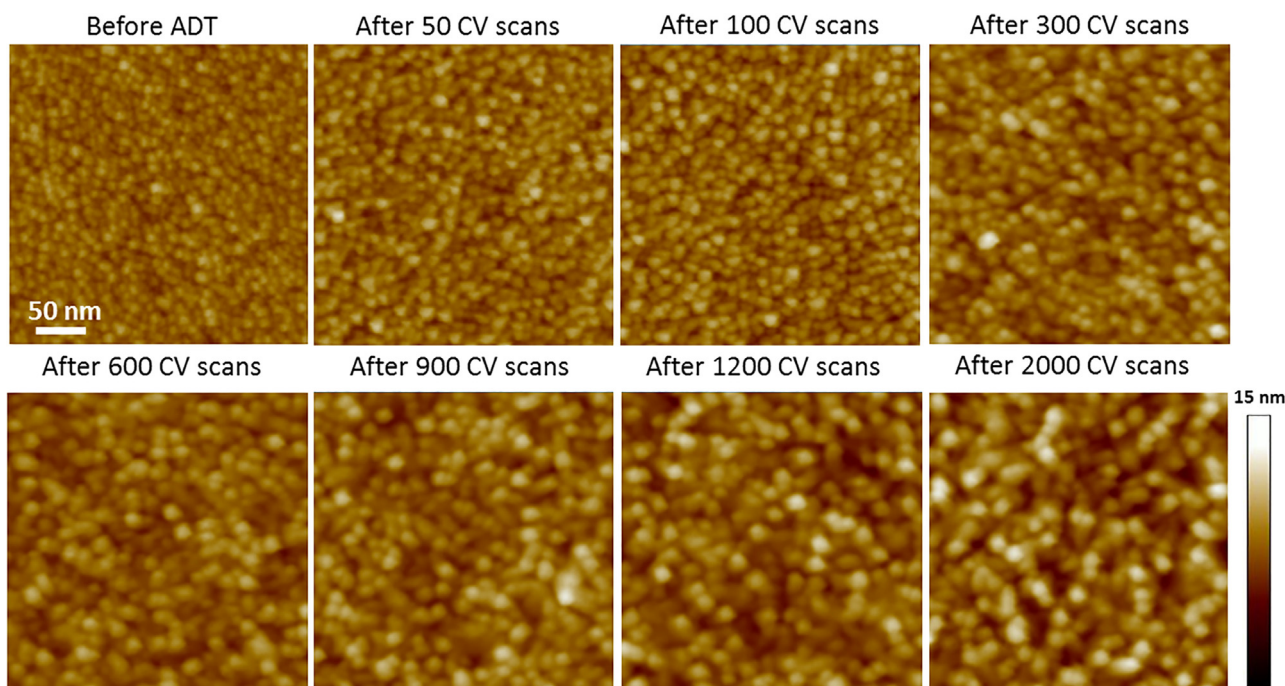

Fig. 3. *In situ* AFM images of the pure Pt catalyst captured during ADT.

3.2. Accelerated durability test

To evaluate the stability of the aforementioned Pt-Ni alloys, the ADTs were conducted. The EC-AFM technique was applied to catalysts films in order to investigate, *in situ*, the morphological changes caused by ADT. We started with pure Pt as the reference sample. In subsequent experiments, with Pt-Ni films, identical protocol was used. Fig. 3 shows the acquired AFM image of the as-deposited Pt (0 CV) together with the same film which underwent 50, 100, 300, 600, 900 1200 and 2000 CV scans within 0 and 1.3 V_{RHE} interval. Each set of AFM images is displayed with fixed Z-contrast in order to better follow changes in morphology. The as-deposited reference Pt sample exhibited homogeneous grainy structure, which is inherent for a sputtered thin film. A gradual coarsening of the Pt film was observed during ADT. The RMS roughness value (R_q), calculated from AFM images, increased from 0.36 nm for the sample prior to cycling to 1.2 nm for the sample after 2000 CV cycles. We associate coarsening effect with the dissolution and redeposition of Pt at higher potentials, leading to the growth of larger Pt nanoparticles due to the Ostwald ripening effect [30,35,36]. Moreover, a contribution of the particle coalescence and detachment from carbon substrate cannot be excluded during the ADT.

Fig. 4 shows the morphological evolution of the as-deposited Pt-Ni films during ADT. One can observe more drastic changes in morphology of Pt-Ni with respect to pure Pt film. The major changes were observed already after the first 50 CV scans, when significant surface cracking of the film occurred, accompanied by slight increase of catalyst's grain size. This effect continues with further increase of CV scans up to 600, after which images remained almost identical, confirming a relative stabilization of the film against further transformations process. The RMS roughness changed drastically, from 0.63 nm for the sample before cycling to 3.2 nm for the sample which underwent 2000 CV cycles. The formation of relatively large cracks can be associated with a Ni leaching, which will be discussed in more detail later. In turn, catalyst film coarsening can be assigned to Ostwald ripening and/ or coalescence likewise in the case of the reference Pt film.

Contrary to the as-deposited Pt-Ni films, the AFM results demonstrated that the annealed Pt-Ni films exhibited a remarkably higher stability (Fig. 5). The changes in morphology during cycling were not so drastic. For this reason, only images prior and after 2000 CV scans are shown in Fig. 5. Only a negligible roughening of the surface can be detected during ADT. The calculated RMS roughness increased from 0.32 nm to 0.96 nm. Furthermore, no large voids were observed in the structure, in contrast to the non-annealed sample (Fig. 4).

To obtain a comprehensive description of processes, which occur during ADT, it is very important to associate the aforementioned morphology changes with cyclic voltammograms measured at the same time. Fig. 6 represents a set of selected CV curves captured simultaneously with AFM images for the pure Pt, as-deposited Pt-Ni and annealed Pt-Ni samples. Additionally, Fig. 7a and b display the comparison of the initial (2nd) and final (2000th) CV curves for all three catalysts.

CV curves recorded on the pure Pt film can be seen in Fig. 6a. Voltammograms exhibit a familiar shape of pure polycrystalline platinum with two pronounced symmetric peaks between 0 and 0.3 V, which correspond to underpotential adsorption/desorption of hydrogen (H_{UPD}) on (110) (more intense) and on (100) (less intense) Pt step sites exposed to the electrolyte (see highlighted
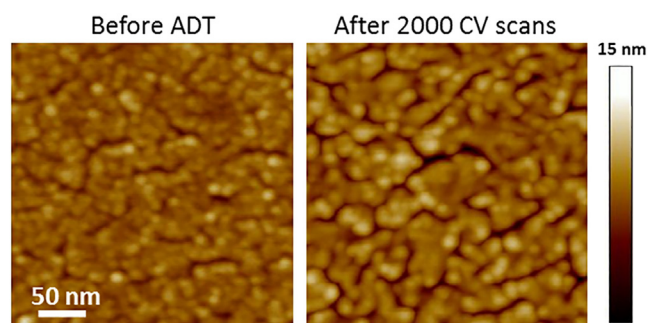

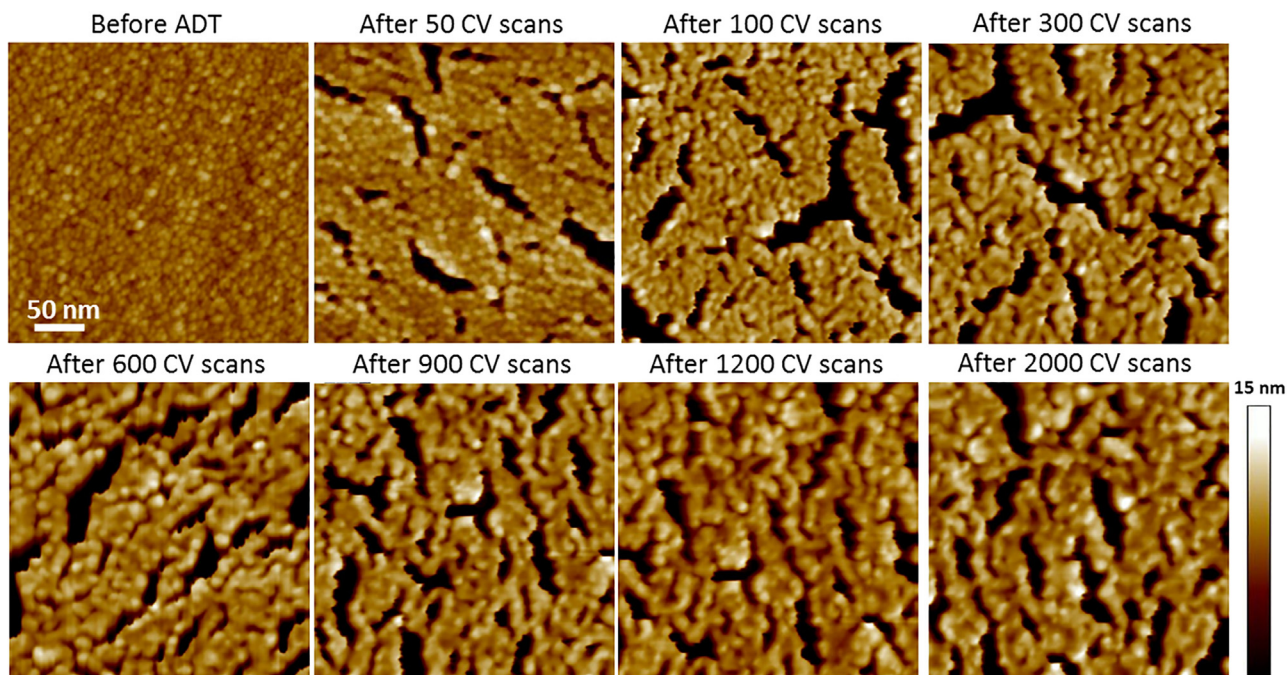**Fig. 5.** *In situ* AFM images of the annealed Pt-Ni catalyst captured during ADT.
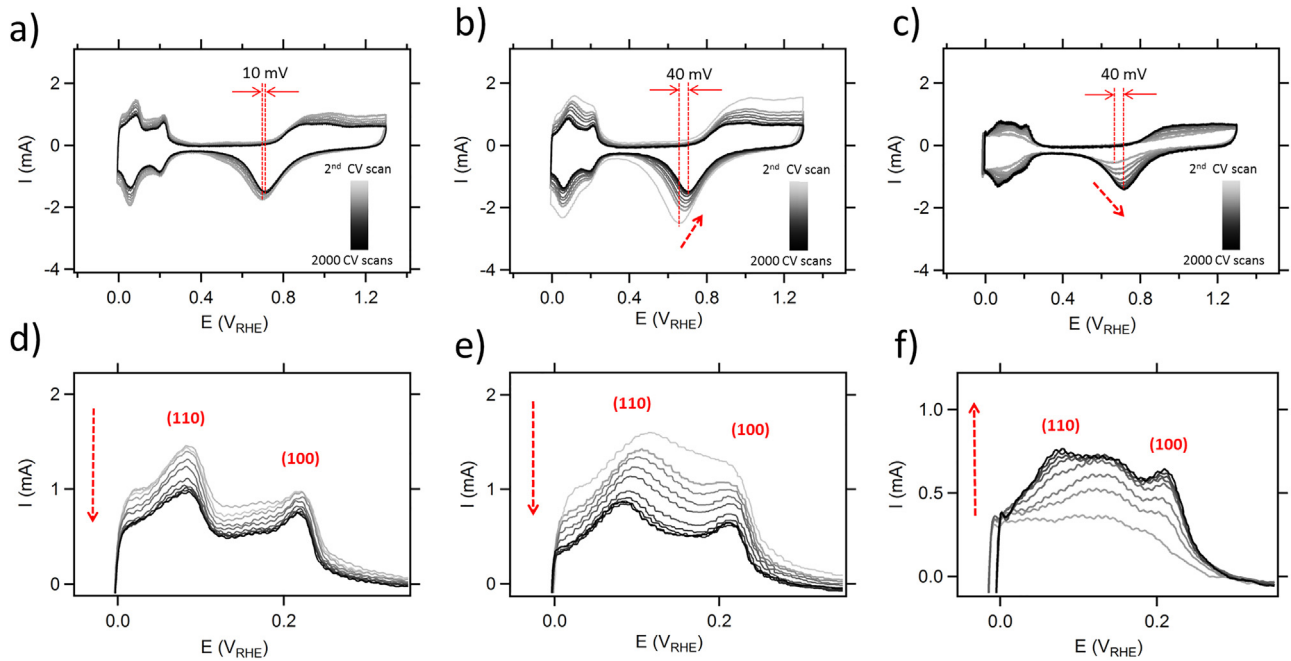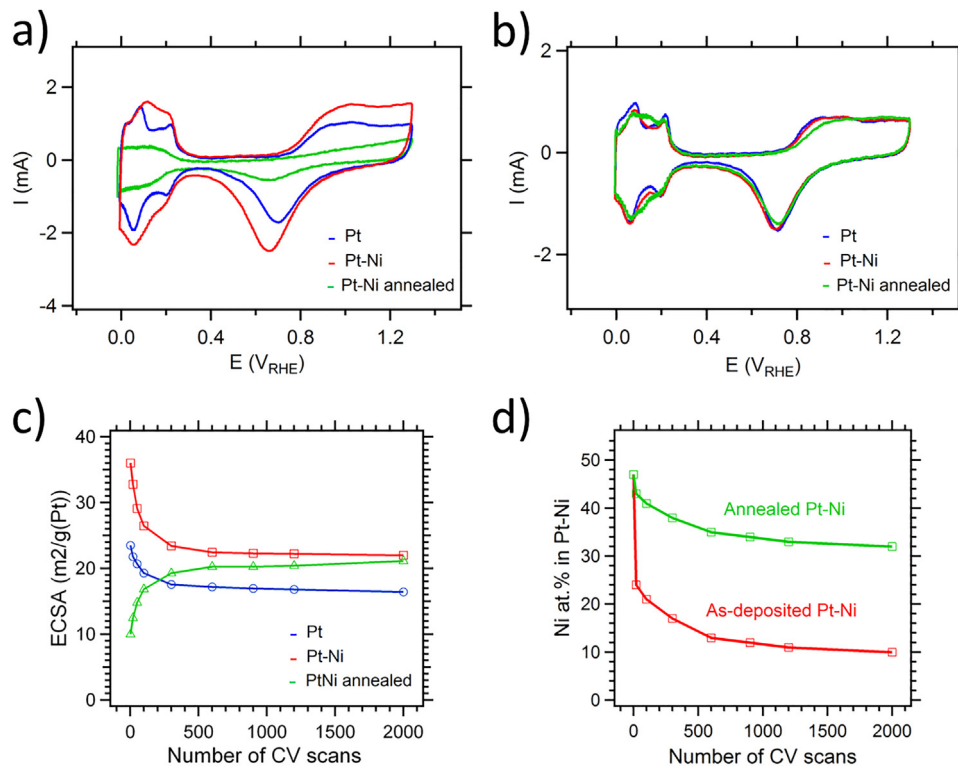

Fig. 4. *In situ* AFM images of the as-deposited Pt-Ni catalyst captured during ADT.

Fig. 6. Selected cyclic voltammograms of (a) pure Pt; (b) as-deposited Pt-Ni; and (c) annealed Pt-Ni during ADT. The H_{UPD} region for (d) pure Pt; (e) as-deposited Pt-Ni; and (f) annealed Pt-Ni highlighted from corresponded voltammograms. Arrows indicate the evolution during the cycling.

Fig. 7. Comparison of (a) initial voltammograms and (b) voltammograms after 2000 CV cycles for the Pt-Ni and Pt films. c) Evolution of ECSA during electrochemical cycling of the Pt and Pt-Ni films. d) Relative nickel atomic concentration in the Pt-Ni thin films as a function of number of CV cycles determined by EDX.

H_{UPD} region in Fig. 6d). The H_{UPD} region is followed by the double layer potential region from 0.3 to 0.5 V. The next fingerprint features are the platinum oxidation/reduction peaks above 0.5 V. The formation of Pt-O occurs in the positive scan direction, starting from approximately 0.8 V. The coverage of Pt-O increases with increasing potential and according to the literature at 1.15 V the

oxidation of the surface should be complete [35]. Further increase of the potential should lead to the place-exchange between Pt and O atoms and formation of bulk oxides [30,35]. This effect is known to be responsible for more severe destruction of Pt surface when cycling to higher potentials. Indeed, a gradual decrease of currents of all featured CV peaks was observed upon cycling. The evolution

of the electrochemically active surface area (ECSA), calculated from the corresponding CV curves, using the charge of H_{UPD} region as a function of cycle number is plotted in Fig. 7c (blue line). The ECSA decreased with the number of CV cycles, with the major drop during the first 600 cycles. With further increase in number of CV cycles the ECSA value remained more or less unchanged. ECSA decrease during the entire ADT was estimated to be about 30% for pure Pt. This phenomenon can be explained by catalyst coarsening measured using AFM (see Fig. 3), which leads to a decrease of the number of electroactive sites responsible for reactions on the surface. Also, a continuous positive shift (10 mV) in the platinum oxide reduction peak at around 0.7 V was observed during ADT. Such small shift could be also assigned to the increase of the grain size as reported previously [37,38].

The set of CV curves for the as-deposited Pt-Ni catalyst captured under identical conditions is shown in Figs. 6b and e. Initial CV shows larger currents over the entire potential window in comparison to pure Pt (see Fig. 7a). Furthermore, no distinguished H_{UPD} peaks were detected. This is a frequently observed phenomenon in the case of Pt-Ni alloys, which do not contain such low-index terminations as pure Pt catalysts and indicates that the adsorption on Pt-Ni is different from that on pure Pt [39]. However, already after the first 50 CV scans, distinct features corresponding to (110) and (100) adsorption sites became resolved (see Fig. 6e). Upon further cycling, the charge under hydrogen region gradually decreased and its shape evolved into a well-defined H_{UPD} profile corresponding to pure Pt. This behavior demonstrates that the redistribution of hydrogen adsorption sites occurs during ADT, apparently due to catalyst dealloying, leading to the formation of Pt-rich surface layers [18,20]. Indeed, the CV curve of Pt-Ni and that of pure Pt are almost identical after entire ADT procedure (see Fig. 7b). The Ni-depleted surface was also confirmed by ex situ XPS and SRPES techniques in Figs. S4a and c, respectively. It can be seen that the Ni 2p peak decreased substantially after 2000 CV cycles according to XPS. Moreover, SRPES showed complete absence of Ni at the top surface of the as-deposited Pt-Ni after ADT.

A significant shift of the Pt-O reduction peak ($\sim$40 mV) towards more positive potentials was identified during ADT (see Fig. 6b). This shift cannot be assigned solely to the morphology changes as suggested above in the case of pure Pt. Hence, it means that adsorption of oxygen and OH groups on the alloy catalyst changes during ADT, apparently due to dealloying.

In Fig. 7c comparison of ECSA time evolution for the pure Pt and as-deposited Pt-Ni films during ADT is shown. The initial ECSA value is much higher for Pt-Ni (36 m^2 g^{-1}) than for pure Pt (23.5 m^2 g^{-1}), which indicates more adsorption sites in the case of the alloy catalyst. On the other hand, the behavior of ECSA during ADT showed similar tendency for both catalysts with a major drop after the first 600 CV cycles and subsequent stabilization. Even though the ECSA remained higher for Pt-Ni (22 m^2 g^{-1}) than for Pt (16.4 m^2 g^{-1}) at the end of ADT, the relative decrease of ECSA during the entire aging test was measured to be about 40%, which is higher than on pure Pt ($\sim$30%), indicating slightly faster degradation of the alloy catalyst.

It has been shown that hydrogen does not adsorb on Ni. As a result, a total H_{UPD} charge should be lower for Pt-Ni than for pure Pt because Ni blocks hydrogen adsorption sites [39]. However, it is important to emphasize that Ni in metallic state is unstable in acidic media at potentials used in fuel cells as well as in our study according to Pourbaix diagram [40,41]. Nickel thus immediately dissolves to electrolyte but, unlike platinum, it cannot redeposit back on the surface due to its low standard redox potential. Consequently, it is reasonable to consider a complete absence of Ni on the as-deposited Pt-Ni alloy surface immediately after the experiment setup at 0 V$_{RHE}$ or during the first few CV cycles. This

Table 1
Pt to Ni atomic ratios in the as-deposited and annealed Pt-Ni before and after ADT calculated using EDX and XRD.

		Before ADT	After ADT
As-deposited Pt-Ni	EDX	$Pt_{0.53}Ni_{0.47}$	$Pt_{0.90}Ni_{0.10}$
	XRD	$Pt_{0.78}Ni_{0.22}$	$Pt_{0.93}Ni_{0.07}$
Annealed Pt-Ni	EDX	$Pt_{0.53}Ni_{0.47}$	$Pt_{0.68}Ni_{0.32}$
	XRD	$Pt_{0.52}Ni_{0.48}$	$Pt_{0.59}Ni_{0.41}$

would explain higher H_{UPD} charge in comparison to pure Pt, as so-called Pt-skeleton is formed on the surface with high concentration of low coordination Pt atoms [9,42]. Unfortunately, this effect cannot be monitored by AFM as it is happening on atomic level, which is below its resolution limit. On the other hand, these low coordination Pt atoms are easier to dissolve at high potentials used in our study. This would enhance Ostwald ripening effect, causing faster decrease of an active surface area of the Pt-Ni catalyst in comparison to the pure Pt during ADT. This is, however, in contrast to previously published results, where acid-treated PtNi/C and the acid-treated/annealed PtNi/C catalysts had only minor losses ($\sim$10%) in ECSA after cycling in comparison to a substantial drop ($\sim$40%) for Pt/C [42]. We assign this difference to higher upper potential limit used in our study, at which the dissolution of Pt was proved to occur [30,35,43].

Contrary to the as-deposited Pt-Ni, the behavior of CVs for the annealed sample during ADT is different (Figs. 6c and f). It is well known that annealing of the films generally leads to a decrease of its surface area due to sintering. Indeed, currents on initial voltammogram were much lower and the double-layer capacitance was narrower in comparison to the non-annealed sample (see Fig. 7a). This is also in consistence with the measured AFM images of the as-deposited and annealed Pt-Ni prior to cycling, shown in Figs. 3 and 4, respectively, where the RMS roughness dropped from 0.63 nm to 0.32 nm upon annealing. The suppressed currents also indicate the formation of Pt-skin type of surface, which is known to be less oxophilic and has significantly reduced number of low-coordination surface atoms [6,9].

The structural transformation of the annealed Pt-Ni during ADT can be followed in more detail in H_{UPD} region, which is highlighted in Fig. 6f. Initial CV shows featureless H_{UPD} region, which is in agreement with previously published results on Pt-skin type Pt-Ni surfaces [6,9]. At the early stages of cycling, the total charges of the hydrogen region arised but no distinct features were resolved in contrast to the non-annealed Pt-Ni sample, where it appeared already after 50 CV scans. Only after 300 CV scans, two additional shoulders, assigned to (110) and (100) adsorption sites on Pt, appeared. Moreover, after the entire ADT, the CV curve for the annealed Pt-Ni had a shape similar to both pure Pt and as-deposited Pt-Ni after ADT, as displayed in Fig. 7b. This is the evidence of Pt-rich surface formation, which was also confirmed by ex situ XPS and SRPES techniques (Figs. S4b and d). At the same time, the platinum reduction peak on the backward sweep exhibited almost the same positive shift as the one for the as-deposited Pt-Ni, indicating similar electrochemical processes occurred on the surface of both samples during aging.

The ECSA behavior for the annealed Pt-Ni films is opposite to the one for the as-deposited Pt-Ni i.e., increasing of ECSA, with the major increase during the first 600 cycles and further saturation and approaching to the ECSA value for the as-deposited Pt-Ni at the end of ADT (Fig. 7c). As was mentioned above, annealing of the films leads to a decrease of its surface area due to sintering which also leads to a decrease of the amount of low-coordinated surface atoms. Moreover, in the case of Pt-skin/Pt-Ni type of surfaces, ECSA value estimated from H_{UPD} peaks was found to be attenuated [10]. These two factors explain much lower ECSA measured for annealed

than that for as-deposited Pt-Ni at the beginning of ADT. The ECSA increase upon cycling for annealed Pt-Ni sample can be associated with gradual destruction of Pt-skin surface.

3.3. Dealloying of as-deposited and annealed Pt-Ni catalyst films during ADT

As it was already suggested above, based on the XPS, SRPES and CV results, changes in morphology and reactions on the surface of Pt-Ni alloy catalysts during ADT occur due to Ni leaching. It is, however, well known that SRPES and XPS are rather surface sensitive techniques, probing only up to 5 nm of catalyst. To further investigate the catalyst dealloying, EDX and XRD analyses were performed.

The concentration of Ni in the as-deposited and annealed Pt-Ni films as a function of cycling number, calculated from EDX spectra is plotted in Fig. 7d. Approximately 80% of Ni was revealed to be etched away during ADT, indicating significant dealloying of the as-deposited Pt-Ni. The film composition changed from $Pt_{0.53}Ni_{0.47}$ to $Pt_{0.90}Ni_{0.10}$ (Table 1). The most significant Ni leaching occurred already during the first 20 CV scans, where about 50% of Ni vanished. Such fast dealloying can be associated with immediate leaching of unprotected Ni with subsequent Pt-skeleton formation as suggested above in the section 3.2 and schematically illustrated in Fig. 8a and b. With further increase in number of cycles, this process continued but it was less pronounced. Due to the fact that Pt is transforming through the electrochemical cycling, more bulk Ni became in contact with electrolyte and dissolves. Such high amount of nickel dissolved to the solution also explains the

formation of large voids in the film during ADT measured by AFM (Fig. 4). Even though alloying with Ni was proved to enhance ORR activity of Pt, it does not survive ADT at harsher condition, which fuel cells may experience at startup/shutdown mode. After such dealloying, the alloy catalyst gradually transforms to almost pure Pt (Fig. 8c).

In case of the annealed sample, however, only about 30% of Ni vanished during ADT, evidencing much higher resistance to corrosion of the annealed films than that of the non-annealed Pt-Ni. The catalyst composition, calculated by EDX, changed from $Pt_{0.53}Ni_{0.47}$ to $Pt_{0.68}Ni_{0.32}$ (Table 1). In contrast to the non-annealed sample, no major concentration drop was observed at the beginning of the ADT. This can be assigned to the Pt-skin type structure of the annealed Pt-Ni, which prevents fast catalyst dealloying at early stages of cycling (see schematic illustration on Fig. 8d). However, during electrochemical cycling to 1.3 V_{RHE} dissolution/redeposition of Pt occurs [30,35,43], which may destabilize the skin layer and thus continuous Ni dissolution takes place during ADT as shown schematically in Fig. 8e. The aforementioned processes for both as-deposited and annealed Pt-Ni became less pronounced when Pt-multilayers surface is formed and protects the Pt-Ni catalyst from further corrosion (Figs. 8c and f).

To further investigate the composition of aged catalysts we compared atomic compositions of the as-deposited and annealed Pt-Ni after ADT calculated using techniques with different probing depth, i.e., SRPES, XPS and EDX. From Table 2 it is clearly evident that in case of both catalysts the top surface does not contain any Ni indicating formation of at least few monolayers of pure Pt. With
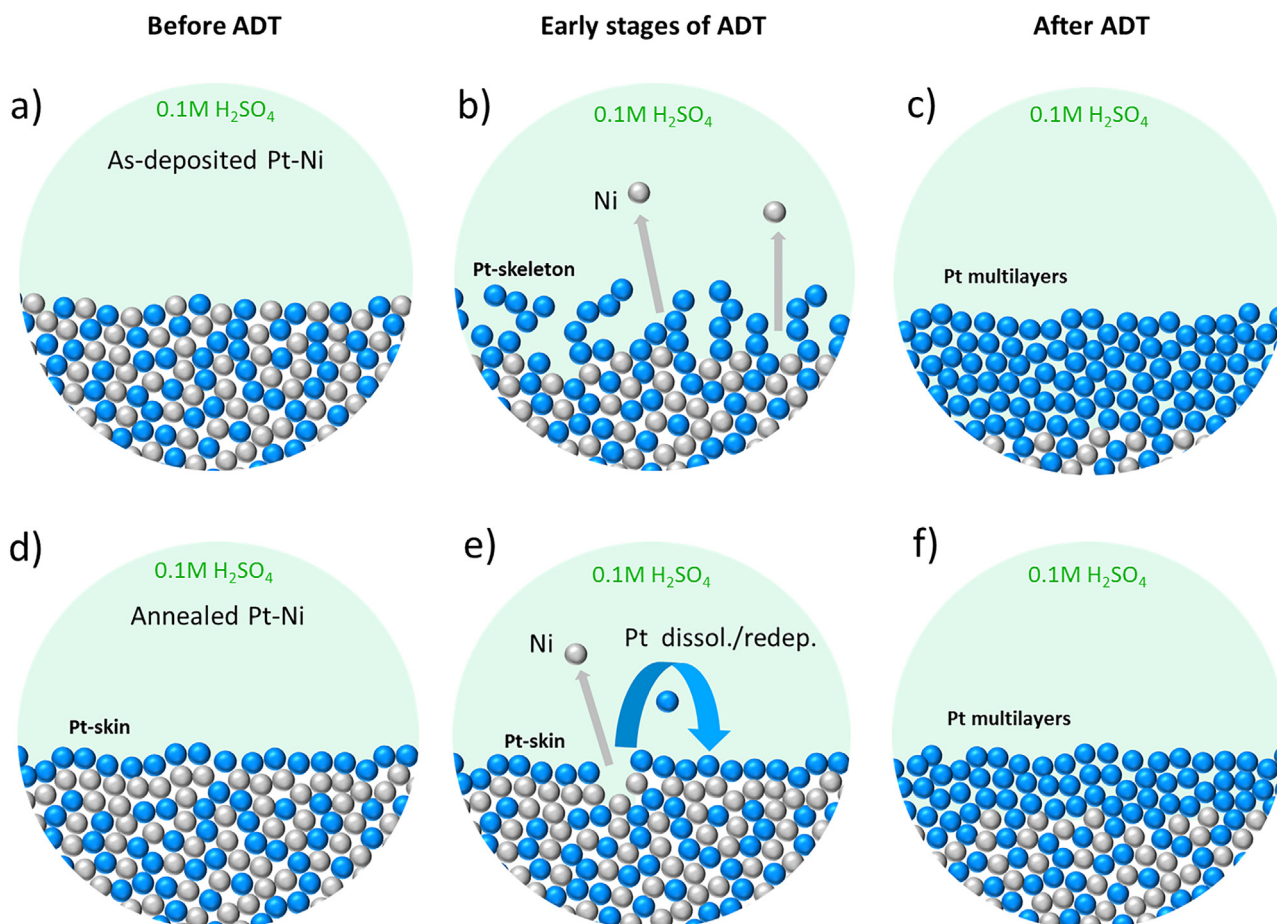

Fig. 8. Schematic illustration of Pt-Ni catalysts dealloying during ADT.

Table 2
Pt to Ni atomic ratios in the as-deposited and annealed Pt-Ni after ADT calculated using SRPES, XPS and EDX.

		As-deposited Pt-Ni after ADT	Annealed Pt-Ni after ADT
Probing depth ↓	SRPES	$Pt_{1.00}Ni_{0.00}$	$Pt_{1.00}Ni_{0.00}$
	XPS	$Pt_{0.95}Ni_{0.05}$	$Pt_{0.85}Ni_{0.15}$
	EDX	$Pt_{0.90}Ni_{0.10}$	$Pt_{0.68}Ni_{0.32}$

increase in probing depth the concentration of Ni increases for both as-deposited and annealed Pt-Ni. However, the differences in bulk composition of investigated samples indicate formation of thicker Pt multilayers in case of as-deposited Pt-Ni than that for annealed one after ADT, as illustrated schematically in Fig. 8c and f.

To get more abundant structure information, the composition of aged films was also extracted from the XRD spectra, shown in Fig. S3. The compositions of the as-deposited Pt-Ni before and after ADT were estimated to be $Pt_{0.78}Ni_{0.22}$ and $Pt_{0.93}Ni_{0.07}$, respectively (Table 1). Comparison with EDX results in Fig. 7d leads to the conclusion that the majority of Ni loss coming from non-alloyed Ni, occurs in the first 20 CV cycles of the ADT. However, even after 20 cycles, Ni leaching continues with operation time, which indicates Ni loss also from the Pt-Ni alloy. Overall, XRD and EDX results showed that ADT leads to severe dealloying of the as-deposited Pt-Ni. For the annealed Pt-Ni catalyst, in turn, the XRD-based compositions before and after ADT were estimated to be $Pt_{0.52}Ni_{0.48}$ and $Pt_{0.59}Ni_{0.41}$, respectively (Table 1). Following repetitive potential cycling, the relative Ni atomic concentration determined from XRD was higher than that from EDX (see Table 1). This reveals the loss of alloyed Ni on the surface and the formation of Pt multilayers on top of Pt-Ni alloy which, in contrast to as-deposited sample, still remains underneath the surface.

In general, severe ADT conditions, which simulate startup/shutdown cycles of a fuel cell, led to deterioration of both catalysts through Ni leaching from the Pt-Ni alloy. The Pt-skin structure of the annealed Pt-Ni mitigates Ni dissolution process, however, it does not eliminate it fully. Even though PtNi alloys were proved to be promising and relatively stable catalyst at steady-state operation mode of a fuel cell, they face significant stability problems during startup/shutdown cycles. Apart from the activity loss of the catalyst due to dealloying, irretrievable Ni dissolution in real fuel cells can cause membrane and catalyst poisoning [44].

4. Conclusions

Pt-Ni thin films were deposited by magnetron co-sputtering on HOPG substrate. We showed that the as-deposited Pt-Ni films were partially oxidized upon exposure to air. After annealing in vacuum Ni-oxides disappeared and the formation of Pt-skin over Pt-Ni catalyst was observed. Moreover, XRD showed higher degree of Ni alloying with Pt for the annealed sample than for the as-deposited one.

Accelerated durability test containing voltage cycling between 0 and 1.3 V_{RHE} was then employed to mimic the startup/shutdown cycles of a fuel cell and investigate stability of the as-deposited and annealed Pt-Ni films. Electrochemical behavior, structure and morphology of catalysts during ADT were systematically investigated using *in situ* EC-AFM in combination with *ex situ* EDX, XPS, SRPES and XRD techniques. The analyses showed that the as-deposited Pt-Ni ages much more rapidly than the annealed one leading to almost complete destruction of the alloy after 2000 cycles of ADT. Better stability of the annealed Pt-Ni likely originates from its Pt-skin structure. Despite better stability of the annealed Pt-Ni alloy it still corrodes because cycling to higher potentials

leads to destruction of Pt-skin due to Pt dissolution/redeposition effect.

Appendix A. Supplementary data

Supplementary data associated with this article can be found, in the online version, at http://dx.doi.org/10.1016/j.electacta.2017.05.202.

References

[1] Handbook of fuel cells: Fundamentals, technology, applications, in: W. Vielstich, A. Lamm, H.A. Gasteiger (Eds.), Wiley, 2003.
[2] J. Greeley, I.E.L. Stephens, A.S. Bondarenko, T.P. Johansson, H.A. Hansen, T.F. Jaramillo, J. Rossmeisl, I. Chorkendorff, J.K. Norskov, Alloys of platinum and early transition metals as oxygen reduction electrocatalysts, Nat. Chem. 1 (2009) 552–556.
[3] T. Toda, H. Igarashi, H. Uchida, M. Watanabe, Enhancement of the electroreduction of Oxygen on Pt alloys with FeNi, and Co, J. Electrochem. Soc. 146 (1999) 3750–3756.
[4] N. Travitsky, T. Ripenbein, D. Golodnitsky, Y. Rosenberg, L. Burshtein, E. Peled, Pt-, PtNi- and PtCo-supported catalysts for oxygen reduction in PEM fuel cells, J. Power Sources. 161 (2006) 782–789.
[5] R. Fiala, M. Vaclavu, M. Vorokhta, I. Khalakhan, J. Lavkova, V. Potin, I. Matolinova, V. Matolin, Proton exchange membrane fuel cell made of magnetron sputtered Pt–CeOx and Pt–Co thin film catalysts, J. Power Sources 273 (2015) 105–109.
[6] V.R. Stamenkovic, B. Fowler, B.S. Mun, G. Wang, P.N. Ross, C.A. Lucas, N.M. Markovic, Improved oxygen reduction activity on Pt3Ni (111) via increased surface site availability, Science. 315 (2007) 493–497.
[7] V. Stamenkovic, B.S. Mun, K.J.J. Mayrhofer, P.N. Ross, N.M. Markovic, J. Rossmeisl, J. Greeley, J.K. Nørskov, Changing the activity of electrocatalysts for oxygen reduction by tuning the surface electronic structure, Angew. Chemie – Int. Ed. 45 (2006) 2897–2901.
[8] M. Vorokhta, I. Khalakhan, M. Václavů, G. Kovács, S.M. Kozlov, P. Kúš, T. Skála, N. Tsud, J. Lavková, V. Potin, I. Matolínová, K.M. Neyman, V. Matolín, Surface composition of magnetron sputtered Pt-Co thin film catalyst for proton exchange membrane fuel cells, Appl. Surf. Sci. 365 (2016) 245–251.
[9] V.R. Stamenkovic, B.S. Mun, K.J.J. Mayrhofer, P.N. Ross, N.M. Markovic, Effect of surface composition on electronic structure, stability, and electrocatalytic properties of Pt-transition metal alloys: Pt-skin versus Pt-skeleton surfaces, J. Am. Chem. Soc. 128 (2006) 8813–8819.
[10] D.F. Van Der Vliet, C. Wang, D. Li, A.P. Paulikas, J. Greeley, R.B. Rankin, D. Strmcnik, D. Tripkovic, N.M. Markovic, V.R. Stamenkovic, Unique electrochemical adsorption properties of Pt-skin surfaces, Angew. Chemie – Int. Ed. 51 (2012) 3139–3142.
[11] J. Durst, M. Lopez-Haro, L. Dubau, M. Chatenet, Y. Soldo-Olivier, L. Guétaz, P. Bayle-Guillemaud, F. Maillard, Reversibility of Pt-skin and Pt-skeleton nanostructures in acidic media, J. Phys. Chem. Lett. 5 (2014) 434–439.
[12] D. Wang, H.L. Xin, R. Hovden, H. Wang, Y. Yu, D. a. Muller, F.J. DiSalvo, H.D. Abruña, Structurally ordered intermetallic platinum–cobalt core–shell nanoparticles with enhanced activity and stability as oxygen reduction electrocatalysts, Nat. Mater. 12 (2013) 81–87.
[13] K.A. Kuttiyiel, K. Sasaki, Y.M. Choi, D. Su, P. Liu, R.R. Adzic, Nitride stabilized PtNi core-shell nanocatalyst for high oxygen reduction activity, Nano Lett. 12 (2012) 6266–6271.
[14] J. Zhang, F.H.B. Lima, M.H. Shao, K. Sasaki, J.X. Wang, J. Hanson, R.R. Adzic, Platinum monolayer on non-noble metal-noble metal core-shell nanoparticles electrocatalysts for O 2 reduction, J. Phys. Chem. B. 109 (2005) 22701–22704.
[15] L. Dubau, M. Lopez-Haro, L. Castanheira, J. Durst, M. Chatenet, P. Bayle-Guillemaud, L. Guétaz, N. Caqué, E. Rossinot, F. Maillard, Probing the structure, the composition and the ORR activity of Pt3Co/C nanocrystallites during a 3422 h PEMFC ageing test, Appl Catal. B Environ. 142–143 (142) (2013) 801–808.
[16] L. Dubau, J. Durst, F. Maillard, L. Guétaz, M. Chatenet, J. André, E. Rossinot, Further insights into the durability of Pt3Co/C electrocatalysts: Formation of hollow Pt nanoparticles induced by the Kirkendall effect, Electrochim. Acta. 56 (2011) 10658–10667.
[17] A. Bonakdarpour, J. Wenzel, D.A. Stevens, S. Sheng, T.L. Monchesky, R. Lobel, R.T. Atanasoski, A.K. Schmoeckel, G.D. Vernstrom, M.K. Debe, J.R. Dahn, Studies of transition metal dissolution from combinatorially sputtered,

nanostructured Pt1-xMx (M = FeNi; 0 < x < 1) electrocatalysts for PEM fuel cells, J. Electrochem. Soc. 152 (2005) A61–A72.

[18] P. Mani, R. Srivastava, P. Strasser, Dealloyed binary PtM3 (M = Cu, Co, Ni) and ternary PtNi3 M (M = Cu, Co, Fe, Cr) electrocatalysts for the oxygen reduction reaction: Performance in polymer electrolyte membrane fuel cells, J. Power Sources. 196 (2011) 666–673.

[19] F.R. Nikkuni, E.A. Ticianelli, L. Dubau, M. Chatenet, Identical-location transmission electron microscopy study of Pt/C and Pt–Co/C nanostructured electrocatalyst aging: Effects of morphological and compositional changes on the oxygen reduction reaction activity, Electrocatalysis 4 (2013) 104–116.

[20] X. Tuaev, S. Rudi, V. Petkov, A. Hoell, P. Strasser, In situ study of atomic structure transformations of Pt-Ni nanoparticle catalysts during electrochemical potential cycling, ACS Nano. 7 (2013) 5666–5674.

[21] K.M. Caldwell, D.E. Ramaker, Q. Jia, S. Mukerjee, J.M. Ziegelbauer, R.S. Kukreja, A. Kongkanand, Spectroscopic in situ measurements of the relative pt skin thicknesses and porosities of dealloyed PtMn (Ni, Co) electrocatalysts, J. Phys. Chem. C. 119 (2015) 757–765.

[22] N. Ishiguro, S. Kityakarn, O. Sekizawa, T. Uruga, T. Sasabe, K. Nagasawa, T. Yokoyama, M. Tada, Rate enhancements in structural transformations of Pt-Co and Pt-Ni bimetallic cathode catalysts in polymer electrolyte fuel cells studied by in situ time-resolved X-ray absorption fine structure, J. Phys. Chem. C. 118 (2014) 15874–15883.

[23] H.R. Colón-Mercado, H. Kim, B.N. Popov, Durability study of Pt3Ni1 catalysts as cathode in PEM fuel cells, Electrochem. Commun. 6 (2004) 795–799.

[24] K. Jayasayee, J.A.R. Van Veen, T.G. Manivasagam, S. Celebi, E.J.M. Hensen, F.A. de Bruijn, Oxygen reduction reaction (ORR) activity and durability of carbon supported PtM (Co, Ni, Cu) alloys: Influence of particle size and non-noble metals, Appl, Catal. B Environ. 111–112 (111) (2012) 515–526.

[25] Y. Choi, H. Mistry, B.R. Cuenya, New insights into working nanostructured electrocatalysts through operando spectroscopy and microscopy, Curr. Opin. Electrochem. 1 (2017) 95–103.

[26] Q. Jia, K.M. Caldwell, K. Strickland, J.M. Ziegelbauer, Z. Liu, Z. Yu, D.E. Ramaker, S. Mukerjee, Improved oxygen reduction activity and durability of dealloyed PtCox catalysts for proton exchange membrane fuel cells: Strain, ligand, and particle size effects, ACS Catal 5 (2015) 176–186.

[27] I. Khalakhan, M. Vorokhta, M. Václavů, B. Šmíd, J. Lavková, I. Matolínová, R. Fiala, N. Tsud, T. Skála, V. Matolín, In-situ electrochemical atomic force microscopy study of aging of magnetron sputtered Pt-Co nanoalloy thin films during accelerated degradation test, Electrochim. Acta. 211 (2016) 52–58.

[28] A. Damian, F. Maroun, P. Allongue, Electrochemical de-alloying in two dimensions: role of the local atomic environment, Nanoscale. 8 (2016) 13985–13996.

[29] Q. Xu, E. Kreidler, T. He, Performance and durability of PtCo alloy catalysts for oxygen electroreduction in acidic environments, Electrochim. Acta. 55 (2010) 7551–7557.

[30] A.A. Topalov, I. Katsounaros, M. Auinger, S. Cherevko, J.C. Meier, S.O. Klemm, K. J.J. Mayrhofer, Dissolution of platinum: Limits for the deployment of

electrochemical energy conversion? Angew. Chemie − Int. Ed. 51 (2012) 12613–12615.

[31] Z. Matěj, A. Kadlecová, M. Janeček, L. Matějová, M. Dopita, R. Kužel, Refining bimodal microstructure of materials with MSTRUCT, Powder Diffr. 29 (2014) S35–S41.

[32] M.C. Biesinger, B.P. Payne, L.W.M. Lau, A. Gerson, R.S.C. Smart, X-ray photoelectron spectroscopic chemical state quantification of mixed nickel metal, oxide and hydroxide systems, Surf. Interface Anal. 41 (2009) 324–332.

[33] A.K. Shukla, M. Neergat, P. Bera, V. Jayaram, M.S. Hegde, An XPS study on binary and ternary alloys of transition metals with platinized carbon and its bearing upon oxygen electroreduction in direct methanol fuel cells, J. Electroanal. Chem. 504 (2001) 111–119.

[34] K. Endo, K. Nakamura, Y. Katayama, T. Miura, Pt-Me (Me = Ir, RuNi) binary alloys as an ammonia oxidation anode, Electrochim. Acta. 49 (2004) 2503–2509.

[35] Y. Sugawara, T. Okayasu, A.P. Yadav, A. Nishikata, T. Tsuru, Dissolution mechanism of platinum in sulfuric acid solution, J. Electrochem. Soc. 159 (2012) F779–F786.

[36] Q. Xu, E. Kreidler, D.O. Wipf, T. He, In situ electrochemical STM study of potential-induced coarsening and corrosion of platinum nanocrystals, J. Electrochem. Soc. 155 (2008) B228–B231.

[37] B.E. Hayden, D. Pletcher, J.-P. Suchsland, L.J. Williams, The influence of support and particle size on the platinum catalysed oxygen reduction reaction, Phys. Chem. Chem. Phys. 11 (2009) 9141–9148.

[38] K.J.J. Mayrhofer, B.B. Blizanac, M. Arenz, V.R. Stamenkovic, P.N. Ross, N.M. Markovic, The impact of geometric and surface electronic properties of Pt-catalysts on the particle size effect in electrocatalysis, J. Phys. Chem. B. 109 (2005) 14433–14440.

[39] V. Stamenković, T.J. Schmidt, P.N. Ross, N.M. Marković, Surface segregation effects in electrocatalysis: Kinetics of oxygen reduction reaction on polycrystalline Pt3Ni alloy surfaces, J.Electroanal. Chem. 554–555 (554) (2003) 191–199.

[40] W.A. Badawy, M.M. El-Rabiee, N.H. Helal, H. Nady, Effect of nickel content on the electrochemical behavior of Cu-Al-Ni alloys in chloride free neutral solutions, Electrochim. Acta. 56 (2010) 913–918.

[41] M. Pourbaix, Atlas of Electrochemical Equilibria in Aqueous Solutions, 2nd English Ed., Natl. Assoc. Corros. Eng., Houston, TX, 1974.

[42] C. Wang, M. Chi, D. Li, D. Strmcnik, D. Van Der Vliet, G. Wang, V. Komanicky, K. C. Chang, A.P. Paulikas, D. Tripkovic, J. Pearson, K.L. More, N.M. Markovic, V.R. Stamenkovic, Design and synthesis of bimetallic electrocatalyst with multilayered Pt-skin surfaces, J. Am. Chem. Soc. 133 (2011) 14396–14403.

[43] I. Khalakhan, J. Lavková, I. Matolínová, M. Vorokhta, V. Potin, P. Kúš, M. Václavů, V.-A. Maraloiu, A.-C. Kuncser, V. Matolín, Electrochemically shape-controlled transformation of magnetron sputtered platinum films into platinum nanostructures enclosed by high-index facets, Surf. Coatings Technol. 309 (2017) 6–11.

[44] J. Durst, M. Chatenet, F. Maillard, Impact of metal cations on the electrocatalytic properties of Pt/C nanoparticles at multiple phase interfaces, Phys. Chem. Chem. Phys. 14 (2012) 13000–13009.